E. A. Repetto

R. Radovitzky

M. Ortiz

Graduate Aeronautical Laboratories,
California Institute of Technology,
Pasadena, CA 91125

R. C. Lundquist

D. R. Sandstrom

The Boeing Company
Mail Stop 7L-25, P. O. Box 3707
Seattle, WA 98124-2207

A Finite Element Study of Electromagnetic Riveting

Electromagnetic riveting, used in some aerospace assembly processes, involves rapid deformation, leading to the finished rivet configuration. Analysis of this process is described for the case of an aluminum rivet joining typical aluminum structural elements. The analysis is based on a finite element method that includes the effects of heating, due to rapid plastic deformation of the material, on the material properties. Useful details of material deformation and thermal history and the final rivet and structure configuration and states of stress and strain are obtained. These results have significant implications in the design, implementation, and improvement of practical fastening processes in the aerospace industry.

1 Introduction

Modern aerospace manufacture employs a variety of fastening techniques. In wing production, aluminum wing skins are riveted to stringers, longitudinal structural elements running from wing root to wing tip. Placement or *upset* of the rivets is accomplished principally by hydraulic tools. However, an electromagnetic rivet upset technology is employed in some processes.

Electromagnetic riveting has the advantage that the equipment is relatively lightweight and portable. In this process, electrical energy stored in capacitors is discharged through a magnet coil, accelerating an armature that carries the rivet die. A similar configuration is applied to both ends of the rivet, balancing the process so that only minor net deflection loads are applied to the structure itself.

The electromagnetic rivet upset process is much faster than the hydraulic, fully deforming the rivet in only 1–2 milliseconds vs. ~0.5 second for hydraulic upset. The corresponding conversion to heat of the plastic work of deformation leads to significant localized heating of the rivet material; indeed, the process appears to be nearly adiabatic. Localized heating is accompanied by thermal softening and the possibility of shear localization. In addition, strain rates in excess of 10^3 sec^{-1} can occur within the material.

Analysis of the rivet upset process is desirable from the point of view of understanding thermal and mechanical history of the materials, and gaining insight into the final configuration of the assembly. Knowing final stresses and strains, and predicting the occurrence of gaps between assembly components are important in assessing durability of the assembly against corrosion effects.

The present paper describes installation of so-called *index head* rivets. These have a *manufactured head* that approximately fits a compound countersink hole in the wing skin structure. Subsequent to rivet upset, a milling process removes the excess head material, leaving a smooth aerodynamic surface on the outside of the wing skin.

The large deformations, combined with the relatively complicated geometry of the index head, countersink, and rivet dies makes analysis of this problem especially demanding. Localized deformation and heating causes strong gradients of the thermal and mechanical parameters. For this reason it was found difficult to obtain satisfactory results with fixed-mesh finite element approaches. The finite element modeling approach described here addresses this issue by employing dynamic remeshing that provides adequate resolution while maintaining a tractable problem dimension.

2 Finite Element Model

We begin with a brief description of the computational framework on which we have based our study of electromagnetic riveting. A more detailed discussion of the computational methodology may be found in [1, 2, 3].

2.1 Dynamics. Electromagnetic riveting is a fast process, with durations in the order of a few *ms*, and consequently it is ideally suited to simulation within an explicit dynamics framework. In addition, the change in shape undergone by the rivet during electromagnetic riveting is quite substantial, which necessitates consideration of large deformation kinematics. We enforce dynamic equilibrium weakly by recourse to the principle of virtual work. Upon finite element discretization, the linear momentum balance equation becomes

$$\mathbf{M}\ddot{\mathbf{x}} + \mathbf{F}^{\text{int}}(\mathbf{x}, \dot{\mathbf{x}}) = \mathbf{F}^{\text{ext}} \tag{1}$$

where $\mathbf{x}$ is the array of nodal coordinates, $\mathbf{M}$ is the mass matrix, $\mathbf{F}^{\text{ext}}$ is the external force array, and $\mathbf{F}^{\text{int}}$ is the internal force array corresponding to the current state of stress. We use the second-order accurate central difference algorithm to discretize (1) in time [4, 5, 6]. Although the minimum time step used in explicit dynamics is bounded by stability [7], contact algorithms available for explicit dynamics are more robust and straightforward than their implicit counterparts. Explicit schemes are therefore more attractive for problems such as electromagnetic riveting which involve complicated contact situations and the total time duration of the process is in the order of milliseconds. Explicit integration is particularly attractive in three-dimensional calculations, where implicit schemes lead to system matrices which often exceed the available in-core storage capacity. Yet another advantage of explicit algorithms is that they are ideally suited for concurrent computing [8].

2.2 Contact. Riveting sets in motion a complex sequence of contact events between several deformable bodies: the dies, the rivet, the skin and the stringer. These complex contact situa-

Contributed by the Manufacturing Engineering Division for publication in the JOURNAL OF MANUFACTURING SCIENCE AND ENGINEERING. Manuscript received April 1997; revised Oct. 1997. Associate Technical Editor: M. Elbestawi.

tions must be effectively resolved during simulation. To this end, we have adopted the contact algorithm developed by Taylor and Flanagan [9] for the PRONTO2D explicit dynamics code. In this approach, the bodies coming into contact can be deformable or rigid. Two contacting surfaces are designated as master and slave surfaces. The method starts by calculating the nodal accelerations from the out-of-balance forces and subsequently computing predictor nodal positions, velocities and accelerations without regard to contact. At the end of this predictor step, some degree of unphysical penetration may have occurred. The requirement of noninterpenetration at the contact zones gives the normal accelerations of the slave nodes, which follow from simple rules of linear momentum balance [3]. A Coulomb friction model may be implemented equally simply. The force that must be applied to the slave node to cancel its relative tangential velocity, i.e., to produce perfect stick, is first computed by linear momentum balance. Then, a tangential frictional force is applied on the surfaces which equals the minimum of the force required for perfect stick and the Coulomb frictional resistance, which completes the algorithm [3]. A balanced master-slave approach in which surfaces alternately act as master and slave is employed. However, rigid surfaces are always treated as master surfaces.

2.3 Thermal Effects. During electromagnetic riveting, substantial amounts of heat may be generated due to the plastic working of the rivet and friction at all the contacting surfaces. The temperatures attained can be quite high [22] and have a considerable influence on the mechanical response. The main sources of heat in our applications are plastic deformation in the bulk and frictional sliding at the interfaces. The rate of heat supply due to the first is estimated as

$$s = \beta \dot{W}^p \tag{2}$$

where $\dot{W}^p$ is the plastic power per unit deformed volume and β is the fraction of plastic work converted into heat. The coefficient β is known to be a strong function of deformation [10] and varies between 0.3 and 1 in aluminum alloys. For simplicity, however, we treat β as a contant. In addition, the rate at which heat is generated at the frictional contact is

$$h = -\mathbf{t} \cdot [\mathbf{v}] \tag{3}$$

where $\mathbf{t}$ is the contact traction and $[\cdot]$ denotes the jump of a field variable across the interface. This heat must be apportioned between the bodies in contact. For simplicity, we assume that the interface is in equilibrium, which implies

$$[T] = 0. \tag{4}$$

This assumption may be justified on the basis of the high contact pressures at the interfaces. Conservation of energy, on the other hand, requires

$$[q] + h = 0 \tag{5}$$

where q is the normal heat flux into the interface. More complete descriptions of the interface allowing for an interfacial conductivity are possible but will not be pursued here.

The temperature distribution in the bulk is governed by the energy balance equation which, upon finite element discretization, furnishes the semi-discrete system of Eq. [6]

$$\mathbf{C}\dot{\mathbf{T}} + \mathbf{K}\mathbf{T} = \mathbf{Q} \tag{6}$$

where $\mathbf{T}$ is the nodal temperature array, $\mathbf{C}$ is the heat capacity matrix, $\mathbf{K}$ is the conductivity matrix, and $\mathbf{Q}$ is the heat source array. In the applications of interest here, the mechanical equations always set the critical time step for stability. It therefore suffices to lump the capacitance matrix and integrate the energy Eq. (6) explicitly by the forward Euler algorithm [4, 5, 6].

The mechanical and thermal field equations are coupled in two different ways. The mechanical response feeds into the thermal equations through the heat generation mechanisms expressed in (2) and (3). The reverse coupling comes from the softening effect of temperature on the yield stress. A staggered procedure [1, 11, 12] is adopted in order to account for this two-way coupling. An isothermal mechanical step is first taken based on the current distribution of temperatures, leading to an update of all mechanical variables. Since the temperatures are held constant throughout this step, they enter the constitutive relations as a parameter (cf. Section 2.4). The heat generated is computed from (2) and (3) and used to compute the heat source array $\mathbf{Q}$ in (6). A rigid-conductor step is then taken at constant mechanical state leading to a new temperature distribution, which completes one application of the algorithm.

2.4 Constitutive Model. In a typical riveting process, very high strain rates may be attained at which the flow stress may exhibit a strong rate-sensitivity [14, 15, 16, 17]. In our calculations we employ the conventional power-law

$$\dot{\epsilon}^p = \dot{\epsilon}_0^p \left[\left(\frac{\bar{\sigma}}{g(\epsilon^p)} \right)^m - 1 \right], \quad \text{if } \bar{\sigma} > g(\epsilon^p) \tag{7}$$

$$\dot{\epsilon}^p = 0, \quad \text{otherwise} \tag{8}$$

where $\bar{\sigma}$ is the effective Mises stress, g the flow stress, ϵ^p the accumulated plastic strain, $\dot{\epsilon}_0^p$ a reference plastic strain rate, and m the strain rate sensitivity exponent. Additionally, we adopt an equally conventional power hardening law in conjunction with Johnson and Cook's [18] power thermal softening law, which gives

$$g = \sigma_y \left[1 - \left(\frac{T - T_0}{T_m - T_0} \right)^\alpha \right] \left(1 + \frac{\epsilon^p}{\epsilon_0^p} \right)^{1/n} \tag{9}$$

where n is the hardening exponent, T the current temperature, T_0 a reference temperature, T_m the melting temperature, α the thermal softening exponent, and σ_y is the yield stress at T_0. The parameters were obtained by curve fitting. We have also included a viscous pressure of the form

$$q = b_1 \rho c_d l \frac{\dot{J}}{J} - \rho \left(l b_2 \frac{\dot{J}}{J} \right)^2, \tag{10}$$

where b_1 and b_2 are constants, c_d is the dilatational wave speed, l a typical element dimension and $\dot{J}/J$ the volumetric strain rate.

We adopt a standard formulation of finite deformation plasticity based on a multiplicative decomposition of the deformation gradient into elastic and plastic components. We employ the fully implicit algorithm of Cuitiño and Ortiz [13] for performing the constitutive updates. Cuitiño and Ortiz' algorithm furnishes a material-independent extension of small-strain updates into the finite deformation range. This considerably simplifies the implementation of the constitutive model just described, which need only be implemented for small strains.

2.5 Adaptive Meshing. A difficulty which is encountered when Lagrangian methods are applied to problems involving unconstrained plastic flow is the severe deformation-induced mesh distortion which is inevitably incurred. This difficulty can be effectively sidestepped by recourse to continuous and adaptive remeshing [1, 2, 3]. Mesh adaption also furnishes an efficient means of resolving multiple scales in the solution with a minimum of degrees of freedom. An effective adaptive meshing capability must address two types of issues: representational, i.e., issues pertaining to the representation of solids; and analytical, including automatic meshing, adaption indicators and mesh-

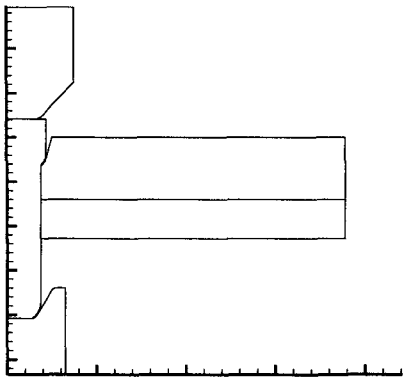

Fig. 1 Boundary representation of the model

to-mesh transfer operators. A few salient issues among these are subsequently addressed in turn.

In calculations we represent solids as hierarchical systems [2, 19, 21, 20]. At the top level, the topological graph points to a set of bodies. A body may in turn comprise several subbodies, e.g., composed of different materials. The boundary of each subbody is decomposed into a collection of closed loops. The loops can be oriented consistently so as to unambiguously define the interior and the exterior of the subbody. Each loop is partitioned into edges. An edge may appear, albeit with different orientations, in the boundaries of two different subbodies. Finally, the geometry of all edges is defined by piecewise quadratic interpolation from a collection of boundary nodes. The use of a sufficiently accurate interpolation of the boundary is essential in order to preserve the mass of the body. A carefully designed solid-modelling procedure is essential in applications involving many evolving and interacting bodies, such as develop in the course of fragmentation simulations [2].

The boundary representation of the model may be taken as a basis for the triangulation of the interior of the solids. The boundary representation serves the additional purpose of specifying the current contact surfaces in the solid. Advancing front methods [21] constitute specially attractive automatic meshing techniques as they require a minimal set of input data—chiefly, the boundary information—from which both elements and interior nodes are generated simultaneously. Triangular elements are introduced one by one from the smallest segment on the front, which is taken as the base of the triangle. In the construction of the initial mesh, the size of the elements is determined by recourse to Jin and Wiberg's [20] control line technique. In this approach, the element size is computed as a weighted average of the boundary element sizes. In subsequent meshes, the size of the new elements inserted at the front is selected in accordance with a prespecified mesh density determined *a posteriori* from the solution. The advancing front algorithm terminates when no segments are left in the front. Carefully designed data structures and search algorithms need to be put in place to ensure an $O(N \log N)$ operation count [23].

In our calculations we employ an h-adaption strategy based on empirical refinement indicators to estimate the optimal mesh density, leading to simultaneous coarsening and refinement [2, 3, 22]. The target mesh density is determined so as to equidistribute certain indicators over all elements in the mesh. The refinement indicators include the bounded deformation norm of the velocity field [22], and the plastic power [2, 3]. For low-hardening metals, these indicators—and others proposed in the literature—are roughly equivalent, and result in refinement (coarsening) in highly active (inactive) regions of the solid. In our implementation, the element size information is interpolated on the old mesh, which serves as a background mesh for the advancing front algorithm.

Where history-dependent materials are concerned, the continuation of the calculations after remeshing requires the transfer to the new mesh of the state variable data. The consistent formulation of transfer operators has been addressed by Ortiz and Quigley [22]. The fundamental question to be ascertained concerns the formulation of consistent finite element equations when all fields at time t_n are supported on a mesh $\mathcal{M}_n$ while the fields at time $t_{n+1} = t_n + \Delta t$ are supported on a different mesh $\mathcal{M}_{n+1}$. Ortiz and Quigley [22] show that, when all finite element representations are introduced into the Hu-Washizu variational principle, the equilibrium and compatibility equations at t_{n+1} follow directly from the interpolation on $\mathcal{M}_{n+1}$. By contrast, the constitutive update giving the state variables on mesh $\mathcal{M}_{n+1}$ is found to comprise two steps. The first step consists of a mapping of the state variables from $\mathcal{M}_n$ onto $\mathcal{M}_{n+1}$. The second step is a conventional state update on $\mathcal{M}_{n+1}$ based on the transferred state variables. Ortiz and Quigley [22] further show that the Hu-Washizu principle unambiguously determines the transfer operator.

3 Electromagnetic Riveting Simulations

In this section, we present selected simulations of electromagnetic riveting carried out within the computational framework described in the foregoing. The particular riveting configuration considered consists of headed rivets and shaped countersinks. The solid model comprises five bodies, namely, the two dies, the skin, the stringer and the rivet. As discussed in Section 2.5, all bodies in the model are defined by their boundaries, Fig. 1. Since the bodies are simply connected, all boundaries consist of one single loop. The loops are further decomposed into edges in order to demarcate salient geometrical features such as sharp corners and abrupt changes in curvature. The edges are subsequently adapted so as to match the target element-size distribution and adequately resolve regions of high curvature. From the boundary representation of the model, an initial mesh is constructed by the advancing front method, Fig. 2. The element size distribution in the interior of the bodies is defined by interpolation of the element size distribution at the boundary, with weights bearing an inverse proportion to the square of the distance to the boundary.

The material constants for the rivet, stringer and skin are collected in Tables 1, 2 and 3, respectively. The dies are idealized as rigid heat conductors, and their thermal properties are listed in Table 4. In view of the short duration of the electromagnetic riveting process, which is of the order of one millisecond, we neglect the transfer of heat through the free surfaces into the environment. By contrast, heat transfer is allowed between all contact surfaces. Since the real load history applied to the dies is not known, we have used one of the forms

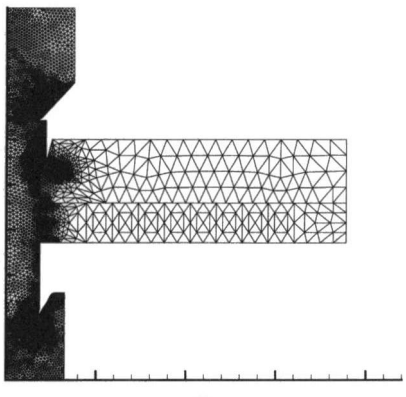

Fig. 2 Initial computational mesh

Table 1 Material parameters, rivet: aluminum 2024

	SI	English
ρ mass density	2700 kg/m^3	0.1 lb/in^3
E Young's modulus	69 GPa	1.0040E+07 lbf/in^2
ν Poisson's ratio	0.33	0.33
σ_y initial yield stress	186.1 MPa	2.7E+04 lbf/in^2
ϵ_0^p reference plastic strain	1E-04	1.E-04
$\dot{\epsilon}_0^p$ reference plastic strain rate	1 s^{-1}	1 s^{-1}
m_1 rate sensitivity exponent	200	200
n hardening exponent	10	10
b_1 bulk viscosity	6E-02	6E-02
b_2 bulk viscosity	1.2	1.2
c heat capacity	920 J/kg K	0.22 BTU/lb-F
k conductivity	188.7 W/m K	0.364 BTU-in/s-ft^2-F
Taylor-Quinney β	0.9	0.9
T_{ref}	293 K	68 F
T_{melt}	993 K	1,328 F
α	1.2	1.2

Table 2 Material parameters, stringer: aluminum 2224

	SI	English
ρ mass density	2700 kg/m^3	0.1 lb/in^3
E Young's modulus	69 GPa	1.0040E+07 lbf/in^2
ν Poisson's ratio	0.33	0.33
σ_y initial yield stress	340 MPa	4.9372E+04 lbf/in^2
ϵ_0^p reference plastic strain	1E-03	1E-03
$\dot{\epsilon}_0^p$ reference plastic strain rate	1 s^{-1}	1 s^{-1}
m_1 rate sensitivity exponent	200	200
n hardening exponent	8	8
b_1 bulk viscosity	6E-02	6E-02
b_2 bulk viscosity	1.2	1.2
c heat capacity	920 J/kg K	0.22 BTU/lb-F
k conductivity	188.7 W/m K	0.364 BTU-in/s-ft^2-F
Taylor-Quinney β	0.9	0.9
T_{ref}	293 K	68 F
T_{melt}	993 K	1,328 F
α	1.2	1.2

Table 3 Material parameters, skin: aluminum 2324

	SI	English
ρ mass density	2700 kg/m^3	0.1 lb/in^3
E Young's modulus	69 GPa	1.0040E+07 lbf/in^2
ν Poisson's ratio	0.33	0.33
σ_y initial yield stress	448 MPa	6.4984E+04 lbf/in^2
ϵ_0^p reference plastic strain	1E-03	1E-03
$\dot{\epsilon}_0^p$ reference plastic strain rate	1 s^{-1}	1 s^{-1}
m_1 rate sensitivity exponent	200	200
n hardening exponent	2	2
b_1 bulk viscosity	6E-02	6E-02
b_2 bulk viscosity	1.2	1.2
c heat capacity	920 J/kg K	0.22 BTU/lb-F
k conductivity	188.7 W/m K	0.364 BTU-in/s-ft^2-F
Taylor-Quinney β	0.9	0.9
T_{ref}	293 K	68 F
T_{melt}	993 K	1,328 F
α	1.2	1.2

Table 4 Material properties, dies: steel

	SI	English
ρ mass density	7800 kg/m^3	0.28 lb/in^3
c heat capacity	480 J/kg K	0.11472 BTU/lb-F
k conductivity	50 W/m K	0.0964 BTU-in/s-ft^2-F
M Mass	8.2 kg	18 lb

$$F(t) = \begin{cases} F_{\max} \sin \pi t/t_0 & t \le t_0 \\ 0 & t > t_0 \end{cases} \tag{11}$$

applied to the far ends of both dies, with $t_0 = 0.5$ ms, and $F_{\max} \approx 278$ kN. In addition to the applied loads, the dies are subject to the contact reactions imparted to them by the rivet. The instantaneous acceleration of the dies then follows from Newton's law as the force resultant acting on the dies divided by their respective masses. As discussed in Section 2.2, the dies are designated as master surfaces as regards the contact algorithm.

Figures 3, 4 and 5 show the adapted mesh, the von Mises equivalent strain and the temperature at the times of maximum travel of the upper and lower dies, and at the final configuration of the rivet just following the springback of the dies, respectively. Details of the computational mesh evolution in the button and head regions are shown in Fig. 6 and 7. Inspection of these figures reveals the ability of the adaptive meshing algorithm to

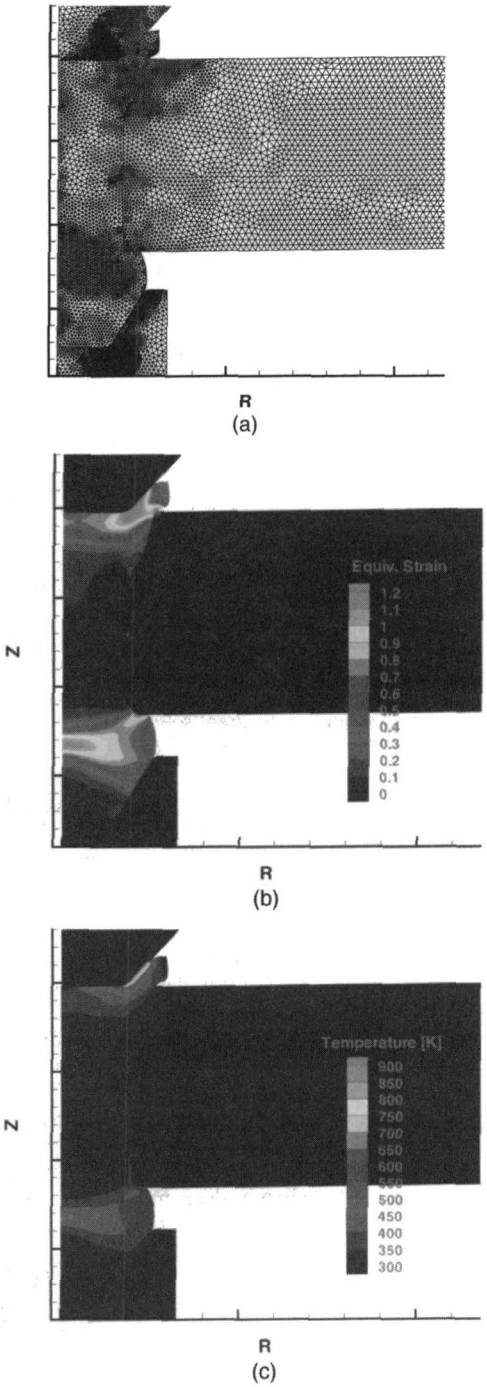

Fig. 3 Solution at the point of maximum travel of the upper die (*a*) adapted mesh (*b*) von Mises equivalent strain (*c*) temperature

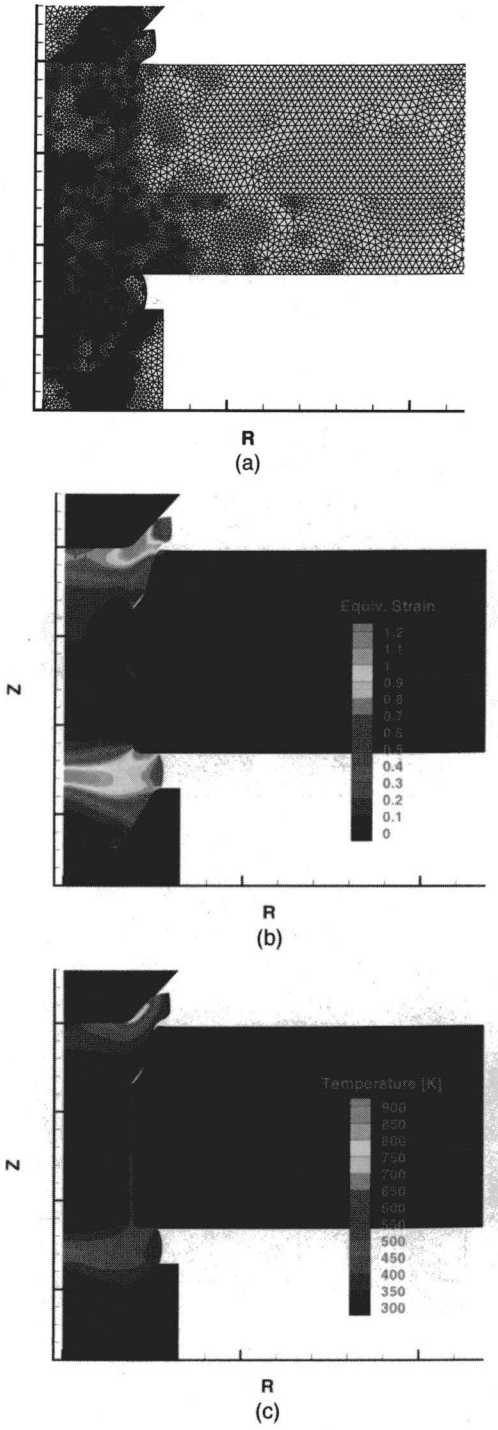

Fig. 4 Solution at the point of maximum travel of the lower die (*a*) adapted mesh (*b*) von Mises equivalent strain (*c*) temperature

preserve the quality of the mesh despite the large deformations incurred. In addition, the adaptive meshing algorithm provides the requisite resolution in regions of intense plastic activity, as desired. The robustness of the contact algorithm is also evident in Fig. 6 and 7, which illustrate the complexity of the contact configurations which develop during the simulation.

As the upsetting of the rivet progresses, the rivet expands laterally due to the Poisson effect and plastic incompressibility. This places the shank of the rivet in tight contact with the skin and the stringer, which results in the sealing of the joint. During the early stages of deformation, when the contact pressure is still building up, the shank slides in the axial direction and a considerable amount of heat is generated at the rivet/skin and rivet/stringer interfaces due to friction. Due to the short duration of the process, this heat does not have sufficient time to diffuse away and a thermal boundary layer develops wherein temperatures of the order of 470 K are attained, Figs. $3(c)$, $4(c)$ and $5(c)$. This temperature rise in turn causes the material to soften and promotes plastic flow. During the later stages of deformation, high contact reactions develop at the rivet/skin and rivet/stringer interfaces which inhibit frictional sliding and result in seizure. This points to the need for accurately controlling the position of the rivet prior to riveting in order to avoid defective heads and buttons. It is also noteworthy how the higher yield

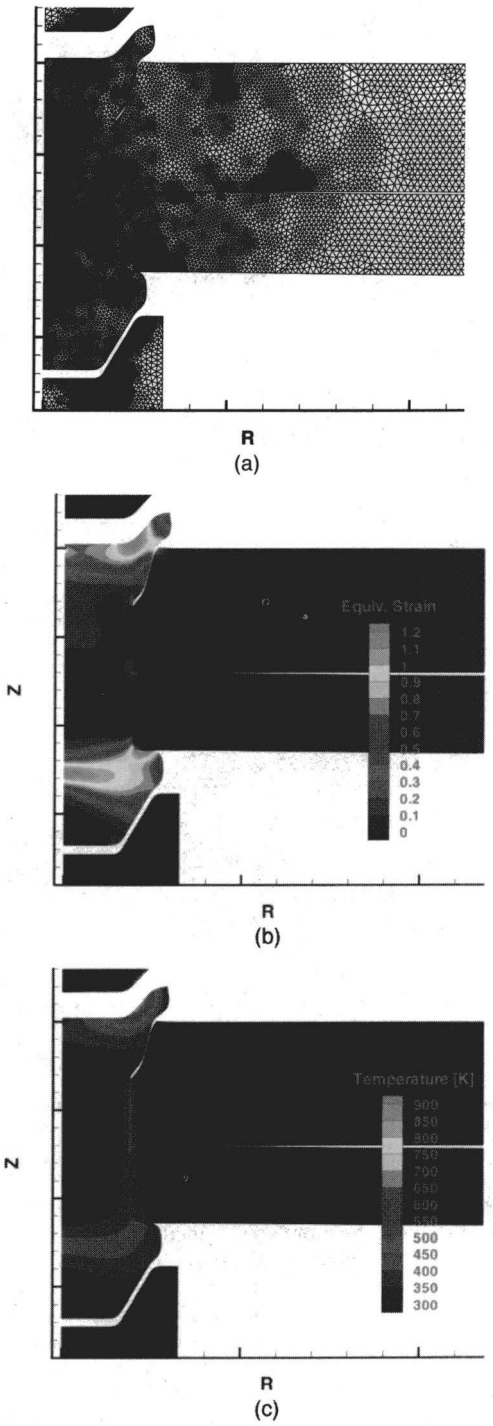

Fig. 5 Final configuration of the rivet upon release of the dies (*a*) adapted mesh (*b*) von Mises equivalent strain (*c*) temperature

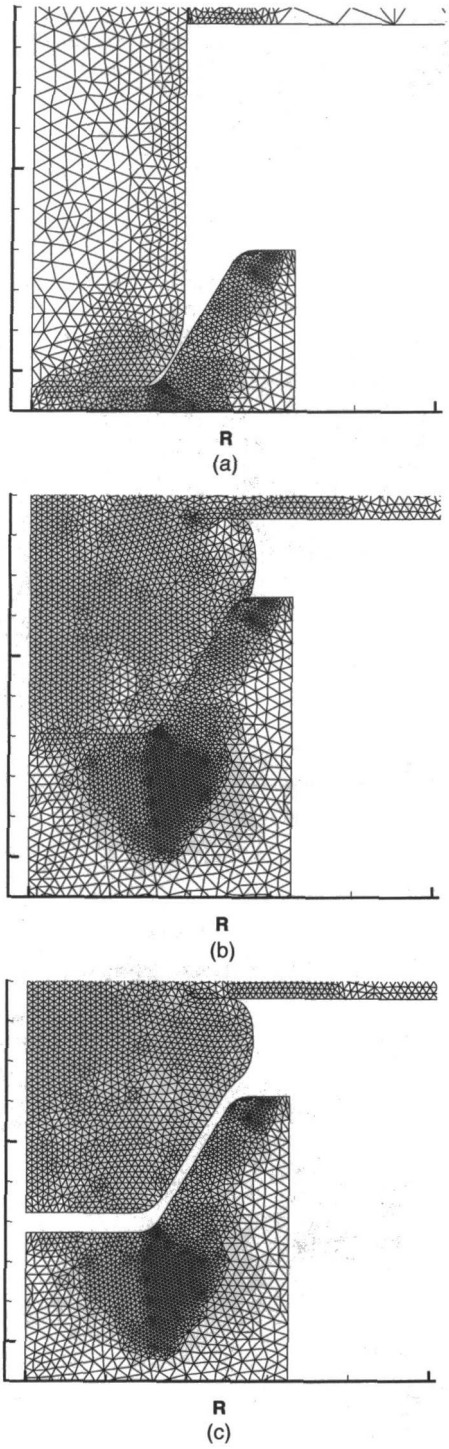

Fig. 6 Detail of the button, stringer and bottom die (*a*) initial mesh (*b*) adapted mesh at maximum die travel (*c*) final configuration

stress of the skin relative to the stringer causes the top section of the rivet shank to be more constrained than the lower section. This results in the formation of a step on the shank at the skin/stringer interface which is observed in practice, Fig. 8.

For the specific riveting configuration under consideration, consisting of headed rivets and shaped countersinks, the head deforms comparatively less than the button. In particular, no shear bands can be discerned in the head region, Figs. 3(*b*), 4(*b*) and 5(*b*). The deformation pattern in the head is reminiscent of a rigid indentation, with large stress and strain concentrations at the corner of the upper die. A jet also forms between the die and the countersink, leading to the formation of a flash. As head material is extruded out, it rubs against the upper die and substantial amounts of heat are generated due to friction. Indeed, the maximum temperatures, of the order of 900 K, arise in this region. By way of contrast, during the early stages of deformation the button material flows radially relative to the shank and a well-developed shear band forms in the intervening space between the two. As the lower die moves up, it confines more of the button increasing the nearly stagnant volume, which makes the shear band narrower.

Following the plastic working of the rivet, skin and stringer, the dies bounce off, due to the elastic response of the system,

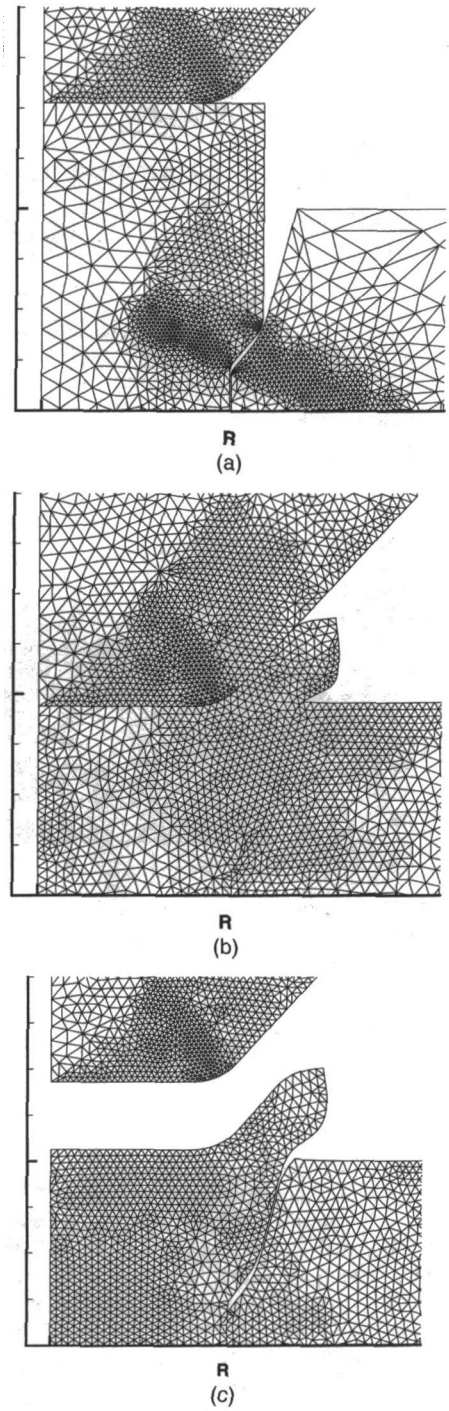

Fig. 7 Detail of the head, skin and top die (*a*) initial mesh (*b*) adapted mesh at maximum die travel (*c*) effect of springback

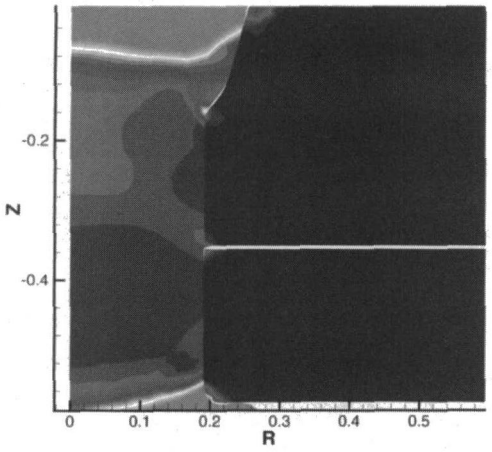

Fig. 8 Detail of corner between rivet and the two metal sheets. Equivalent strains showing a small step due to the different material properties of the components.

and lose contact with the rivet. The computed trajectory of the dies are shown in Fig. 9. The initial upsetting stage and subsequent springback are evident in this figure. The asymmetry of the upper and lower die trajectories, which causes the skin and stringer to bend, is also noteworthy. A symmetric process could be obtained by imposing different loading functions on the lower and upper dies, but this possibility will not be pursued

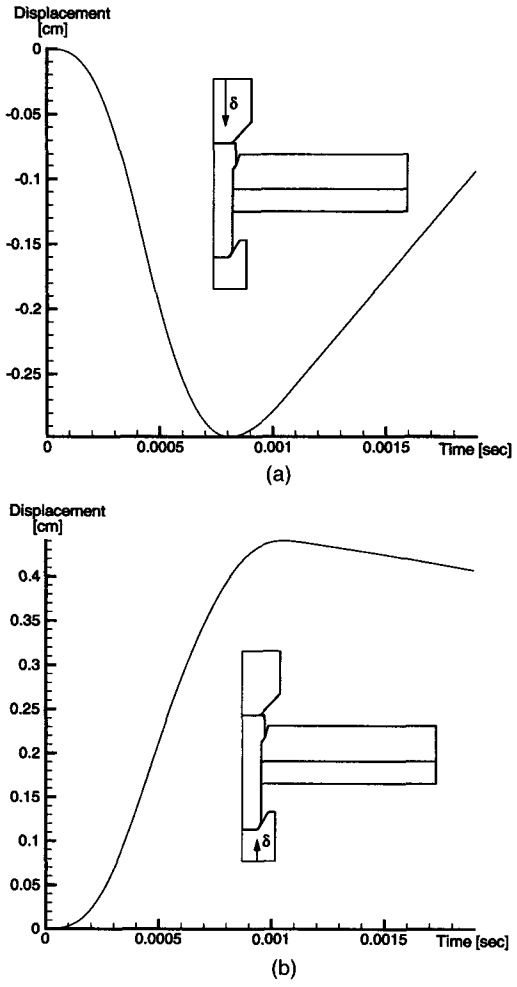

Fig. 9 Computed trajectories of (*a*) upper die (*b*) lower die

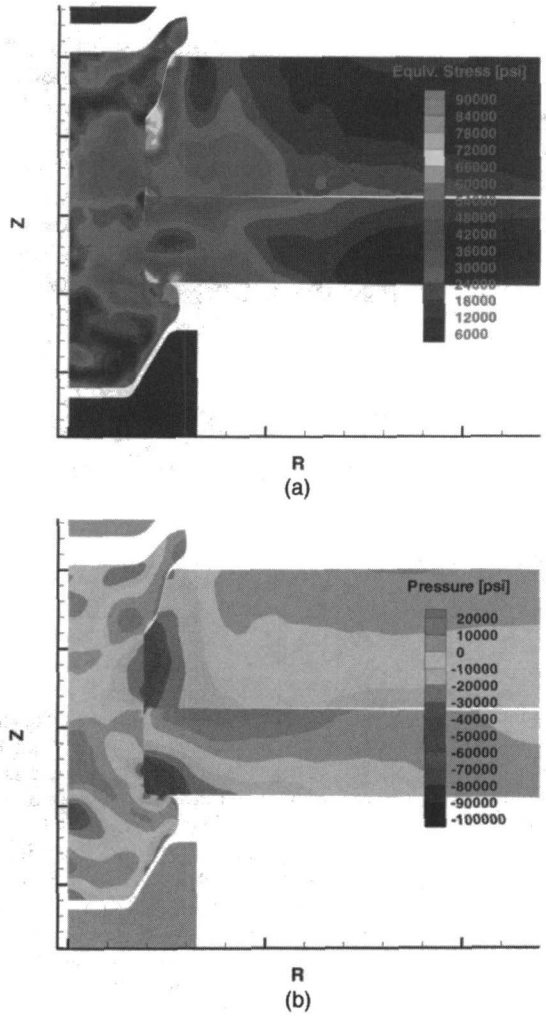

Fig. 10 Residual stresses at the end of the analysis (*a*) von Mises equivalent stress (*b*) pressure

here. Following the release of the rivet, a complex residual stress field becomes established, Figs. 10. It bears emphasis that the computation of these residual stresses, and the attendant springback of the structure, requires the modelling of the elastic response of the material. These important aspects of the solution are accessible to our lagrangian formulation, but not to rigid-plastic formulations. One far-reaching consequence of the springback is the loss of contact between skin and stringer and, most critically, between head and countersink, Figs. 7(*b*) and 7(*c*). A measure of the rivet's confinement may be obtained by removing the skin/stringer structure and letting the rivet expand freely. The resulting radial displacements are shown in Fig. 11.

4 Discussion

The model approach described here has limitations that could affect its utility in the design and development of practical processes. One of these is the assumption of thermal equilibrium at the rivet-structure interface, Eq. (4). This is likely to be an oversimplification because the rivets typically receive an anodize coating prior to assembly. Even under the high pressures present during upset, this could impose a thermal barrier at the interface.

Because axial and lateral alignment of the electromagnetic riveter armatures acting on the two ends of the rivet is imperfect, real systems do not meet the full requirements of axial symmetry, assumed here. A fully three-dimensional treatment of the

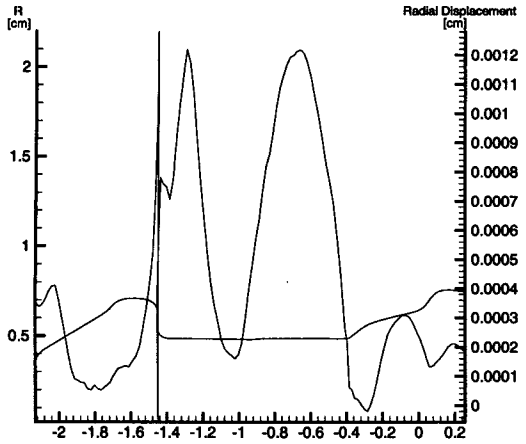

Fig. 11 Rivet radial expansion upon removal of skin/stringer structure

problem would be required for examination of the sensitivity of the solutions to practical alignment issues.

A further limitation is the fact that the load history given in Eq. (11) is only an approximation to the actual loads imposed in practice. Work is in progress to determine actual load histories appropriate to this problem to greater precision.

In spite of these limitations, the analysis approach presented here shows great promise for predicting the performance of practical processes. For instance, it is able to expose details like the gap observed to open up between the head and countersink (c.f. Figs. 7 and 8). Such detail is a valuable indicator of process performance, because gaps could permit moisture entry leading to corrosion. Gap elimination is a major requirement of process design and control.

Test procedures employed in the study of rivet upset processes include sectioning of finished rivets followed by dimensional and surface finish measurements, and metallographic examination. We have also performed neutron diffraction studies of the elastic strain field present in finished rivets. In general, the characteristics of rivet upset predicted by this study are in accord with those determined by these test procedures. However, we have not yet conducted critical validation studies that would quantitatively establish the level of fidelity of the present model results.

Acknowledgments

Eduardo Repetto, Raúl Radovitzky and Michael Ortiz gratefully acknowledge the financial support of The Boeing Company. The authors thank Paul Field and Michael Hyatt for a critical review of the manuscript.

5 References

1 Marusich, T. D., and Ortiz, M., "Modelling and Simulation of High-Speed Machining," *Int. J. Numer. Meth. Engr.,* Vol. 38, 1995, pp. 675–3694.

2 Camacho, G. T., and Ortiz, M., "Computational Modelling of Impact Damage and Penetration f Brittle and Ductile Solids," *Int. J. Solids Structures,* Vol. 33, pp. 20–22, 1996, pp. 2899–2938.

3 Camacho, G. T., and Ortiz, M., "Adaptive Lagrangian Modelling of Ballistic Penetration of Metallic Targets," *Comp. Meth. Appl. Mech. Engr.,* 1996, in press.

4 Hughes, T. J. R., "The Finite Element Method," Prentice Hall, 1987.

5 Hughes, T. J. R., and Belytschko, T., "A Précis of Developments in Computational Methods for Transient Analysis," ASME *Journal of Applied Mechanics,* Vol. 50, 1983, pp. 1033–1041.

6 Belytschko, T., "An Overview of Semidiscretization and Time Integration Procedures," T. Belytschko and T. J. R. Hughes, eds., *Computational Methods for Transient Analysis,* North-Holland, 1983, pp. 1–65.

7 Hughes, T. J. R., "Analysis of Transient Algorithms with Particular Reference to Stability Behavior," T. Belytschko, and T. J. R. Hughes eds., *Computational Methods for Transient Analysis,* North-Holland, 1983, pp. 67–155.

8 Mathur, K. K., Needleman, A., and Tvergaard, V., "Dynamic 3D Analysis of the Charpy V-Notch Test," *Modelling Simul. Mater. Sci. Eng.,* Vol. 1, 1993, pp. 467–484.

9 Taylor, L., and Flanagan, D., "PRONTO 2D: A Two-Dimensional Transient Solid Dynamics Program," Sandia National Laboratories, SAND86-0594, 1987.

10 Hodowany, J., Ravichandran, G., and Rosakis, A. E., work in progress.

11 Park, K. C., and Felippa, C. A., "Partitioned Analysis of Coupled Systems," T. Belytschko and T. J. R. Hughes, eds., *Computational Methods for Transient Analysis,* North-Holland, 1983, pp. 157–219.

12 Lemonds, J., and Needleman, A., "Finite Element Analysis of Shear Localization in Rate and Temperature Dependent Solids," *Mechanics of Materials,* Vol. 5, 1986, pp. 339–361.

13 Cuitiño, A. M., and Ortiz, M., "A Material-Independent Method for Extending Stress Update Algorithms from Small-Strain Plasticity to Finite Plasticity with Multiplicative Kinematics," *Engineering Computations,* Vol. 9, 1992, pp. 437–451.

14 Klopp, R. W., Clifton, R. J., and Shawki, T. G., "Pressure-Shear Impact and the Dynamic Viscoplastic Response of Metals," *Mechanics of Materials,* Vol. 4, 1985, pp. 375–385.

15 Clifton, R. J., and Klopp, R. W., "Pressure-Shear Plate Impact Testing," *Metals Handbook Ninth Edition,* Vol. 8, 1985, pp. 230–239.

16 Tong, W., Clifton, R. J., and Huang, S., "Pressure-Shear Impact Investigation of Strain rate History Effects in Oxygen-Free High-Conductivity Copper," *J. Mech. Phys. Solids,* Vol. 40, 1992, pp. 1251–1294.

17 Zhou, M., Clifton, R. J., and Needleman, A., "Shear Band Formation in a W-Ni-Fe Alloy under Plate Impact," Tungsten & Tungsten Alloys—1992, Metal Powder Industries Federation, Princeton, N.J.

18 Johnson, G. R., and Cook, W. H., "Fracture Characteristics of Three Metals Subjected to Various Strains, Strain Rates, Temperatures and Pressures," *Engng Fract. Mech.,* Vol. 21, 1985, pp. 31–48.

19 Baehmann, P. L., Wittchen, S. L., Shephard, M. S., Grice, K. R., and Yerry, M. A., "Robust, Geometrically Based, Automatic Two-Dimensional Mesh Generation," *Int. J. Num. Meth. Engr.,* Vol. 24, 1987, pp. 1043–1078.

20 Jin, H., and Wiberg, N. E., "Two-Dimensional Mesh Generation, Adaptive Remeshing and Refinement," *Int. J. Num. Meth. Engr.,* Vol. 29, 1990, pp. 1501–1526.

21 Peraire, J., Vahdati, M., Morgan, K., and Zienkiewicz, O. C., "Adaptive Remeshing for Compressible Flow Computations," *J. Comp. Phys.,* Vol. 72, 1987, pp. 449–466.

22 Ortiz, M., and Quigley, IV, J. J., "Adaptive Mesh Refinement in Strain Localization Problems," *Comp. Meth. in Appl. Mech. Engng.,* Vol. 90, 1991, pp. 781–804.

23 Lohner, R., "Some Useful Data Structures for the Generation of Unstructured Grids," *Comm. Appl. Numer. Meth.,* Vol. 4, 1988, pp. 123–135.